

# Dynamical evolution of the spectator systems produced in ultra-relativistic heavy-ion collisions

K. Mazurek,<sup>1,\*</sup> A. Szczurek,<sup>1,†</sup> C. Schmitt,<sup>2,‡</sup> and P.N. Nadtochy<sup>3,§</sup>

<sup>1</sup>*Institute of Nuclear Physics PAN, ul. Radzikowskiego 152, PL-31342 Kraków, Poland*

<sup>2</sup>*Institut Pluridisciplinaire Hubert Curien, 23 rue du Loess, B.P. 28, F-67037 Strasbourg Cedex 2, France*

<sup>3</sup>*Omsk State Technical University, Mira prospekt 11, Omsk, 644050, Russia*

(Dated: March 12, 2022)

In peripheral heavy-ion collisions at ultra-relativistic energies, usually only parts of the colliding nuclei effectively interact with each other. In the overlapping zone, a fireball or quark-gluon plasma is produced. The excitation energy of the heavy remnant can range from a few tens to several hundreds of MeV, depending on the impact parameter. The decay of these excited spectators is investigated in this work for the first time within a dynamical approach based on the multi-dimensional stochastic Langevin equation. The potential of this exploratory work to understand the connection between electromagnetic fields generated by the heavy spectators and measured pion distributions is discussed.

PACS numbers: 21.60.-n, 21.10.-k, 24.75.+j, 25.70.Gh

## I. INTRODUCTION

Collisions between heavy ions flying with ultra-relativistic velocities are studied theoretically and experimentally since many years, with the main goal being the study of the properties of the quark-gluon plasma (QGP). In the present work, the attention is devoted to the properties and decay of the heavy remnants of the collision. Non-central collisions unambiguously lead to azimuthal asymmetries in the pion trajectory [1], which may be linked to the electromagnetic field generated by these fast-moving charged remnants. The influence of this field on charged pions was discussed in [2, 3].

Previous work confirmed that the collision between two heavy ions at (ultra-)relativistic energy can be viewed as a two-step process. The first stage of the collision, often referred to as abrasion, is a very fast process. The two remnants of the collision are considered as 'spectators': They are characterized by some mass deficit as compared to the mass of the reaction partners, but follow their initial path almost undisturbed. In the (participant) collision zone, at typical CERN Super Proton Synchrotron (SPS) energies, pions or other hadrons are produced and form a quark-gluon plasma. The mass of the spectator remnants, and accordingly the number of nucleons involved in the fireball, depend on the impact parameter. The second stage of the collision, in comparison to the first one, is a slow process. Along this stage, often referred to as ablation, the primary hot products release their excitation energy and decay to a stable state

by emitting light particles and  $\gamma$ -rays. Heavy spectators have additionally a large probability to decay by fission. During this time, the fireball expands and produced particles (mostly pions) which fly apart.

The fireball was discussed in the context of the abrasion model already in [4–6]. A new calculation [7], based on simple Coulomb effects, suggests that at SPS energies the QGP plasma creates a kind of fire-streaks, which velocity along the collision axis changes across the impact parameter space. It is assumed that the spectators do not feel the interaction with the plasma. Also, it is believed that the decay of the spectators is unimportant for the evolution of the QGP and subsequent hadronization. However, the strong electromagnetic field generated by fast-moving spectators can act *e.g.* on the charged pions created from the fire-streaks of the QGP. Electromagnetic effects yield different distortions of the positively and negatively charged pions. They lead to a damping of  $\pi^+$  and an enhancement of  $\pi^-$  for pions moving with velocity equal to the velocity of the spectators. Long-range electromagnetic interactions [2] are possible provided that spectators live long enough. Consequently, a realistic estimate of this time, and understanding of what happens not only to the plasma but also to the spectators, seems interesting and important in this context.

While previous works focused on the plasma, the present study is dedicated to the properties and decay of the heavy spectators. Our approach consists in two steps. First, the properties, in terms of size and excitation energy, of the remnants of the collision are compared as obtained in three different abrasion models. In a second step, the decay of the remnants is computed within a dynamical model based on the Langevin approach. Various de-excitation channels are open to the decay of the highly-excited systems produced in the first stage of the collision, going from light-particle evaporation, intermediate-mass fragment (IMF) emission, fis-

\*Electronic address: Katarzyna.Mazurek@ifj.edu.pl

†Electronic address: Antoni.Szczurek@ifj.edu.pl

‡Electronic address: christelle.schmitt@iphc.cnrs.fr

§Electronic address: nadtoch77@gmail.com

sion, multifragmentation, and up to vaporisation. In the present model, the Langevin code is restricted to the spectator decay by evaporation and fission. Other channels are not treated here. The dynamical results are compared to the predictions by the abrasion-ablation statistical model ABRABLA [8, 9] which has shown successful in predicting the spectator decay in the beam energy range from about 100 to several thousands of MeV/nucleon. As a test case for our new dynamical framework, we study the reaction  $^{208}\text{Pb}+^{208}\text{Pb}$  at 158 GeV/nucleon energy ( $\sqrt{s_{NN}} = 17.3$  GeV) measured at the CERN SPS at various centralities [10], and for which electromagnetic distortions were observed in the kinematical pion distributions.

## II. ABRASION MODELS

The first stage of the collision between two heavy ions at ultra-relativistic energies ( $\sqrt{s_{NN}} \geq 5$  GeV) is very fast and energetic. As mentioned above, so far not much attention was paid to the description of the spectator decay. According to the suggested importance of the time evolution of the latter [2] on pion trajectories, we focus on this aspect. Since the system considered in the study ( $^{208}\text{Pb}+^{208}\text{Pb}$ ) is symmetric, the de-excitation of one remnant (from either the projectile, or the target), only, has to be explicitly computed. The calculation can, of course, easily be generalized to asymmetric entrance channels.

Three different abrasion models are proposed including, with increasing sophistication: a purely geometrical and macroscopic picture based on the Liquid Drop Model (LDM), the abrasion model ABRA of Gaimard and Schmidt [8], and the microscopic theory of Glauber [11]. The masses and excitation energies as predicted for the heavy remnant (hereafter prefragment or spectator) as a function of impact parameter in these three models are first compared. Next, they are used as the input for the calculation of its decay.

We note that the abrasion picture is valid for beam velocities larger than the Fermi velocity. Its upper limit of applicability was never tested to our knowledge. Thus, the present work is also an interesting exploratory investigation in this respect.

### A. Geometrical macroscopic approach

Right after the collision the spectator prefragment can experience a very exotic shape, which relaxes quickly towards a spherical configuration. In the here-proposed simplest approach, the excitation energy of the prefragment is equal to the Liquid Drop deformation energy [4], calculated as the difference between the liquid drop energy of the deformed and spherical shapes.

$$E^* = E_{LDM}(\text{deformed spectator})$$

$$-E_{LDM}(\text{spherical spectator}), \quad (1)$$

The crucial point is the calculation of the surface energy of the possibly exotic prefragment shapes as a function of impact parameter  $b$ , defined as the distance between the centers of the colliding nuclei. Depending on  $b$ , the way the aforementioned cut-off takes place may be different. Three scenarios are considered for determining the shape of the remnant of the collision. Its volume (equivalently, mass) is directly related to the number of nucleon removed or 'abraded', assuming a constant nuclear matter density. The Unchanged Charge Density (UCD) assumption is further used to determine its neutron and proton numbers according to:  $A_{\text{initial}}/Z_{\text{initial}} = A_{\text{spectator}}/Z_{\text{spectator}}$ , where the subscript *initial* refers to the projectile (equivalently, target).

Let us consider the simple geometrical situation of a sphere cut off by a plane (hereafter 'sphere-plane'). Then the final shape resembles a sphere without spherical dome. The corresponding form can be described as follows:

$$S(\text{sphere}) = \{(\rho, z, \phi) : 0 \leq z \leq R, \\ 0 \leq \rho \leq \sqrt{R^2 - z^2}, 0 \leq \phi \leq 2\pi\} . \quad (2)$$

The spherical cap:

$$W = \{(\rho, z, \phi) : b \leq z \leq R, \\ 0 \leq \rho \leq \sqrt{R^2 - (b+z)^2}, 0 \leq \phi \leq 2\pi\} . \quad (3)$$

The deformed spectator:

$$\Omega = S(\text{sphere})/W; . \quad (4)$$

The volume of the spectator in 'sphere-plane' scenario:

$$V_{\Omega} = \int \int_{S(\text{sphere})/W} dV(\rho, z, \phi) \\ = \int_0^{2\pi} d\phi \int_0^b dz \int_0^{\sqrt{R^2 - z^2}} d\rho \quad (5)$$

and the surface:

$$S_{\Omega}(b) = 2\pi \int_0^b dz \sqrt{R^2 - z^2} . \quad (6)$$

The volume of the spherical cap:

$$V_W = \int \int_W dV(\rho, z, \phi) \\ = \int_0^{2\pi} d\phi \int_b^R dz \int_0^{\sqrt{R^2 - (b+z)^2}} \rho d\rho, \quad (7)$$

where  $S$  is the surface of the sphere with radius  $R$  and  $dS$  is a two-dimensional differential element of the sphere volume. The surface of the sphere described by the function:  $x^2 + y^2 + z^2 = R^2$  cut by the plane  $z = b$  is calculated

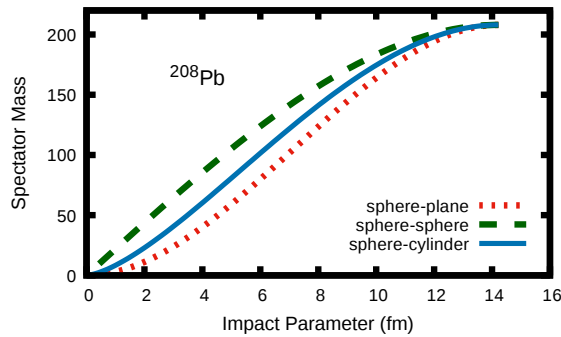


FIG. 1: (Color on-line) Mass of the spectator produced in three geometrical scenarios described in the text as a function of the impact parameter for  $^{208}\text{Pb}+^{208}\text{Pb}$  collisions.

as:

$$\begin{aligned}
 S(def) &= \int \int_D \sqrt{1 + \left(\frac{\partial z}{\partial x}\right)^2 + \left(\frac{\partial z}{\partial y}\right)^2} dx dy \\
 &= \int_{-\sqrt{R^2-b^2}}^{\sqrt{R^2-b^2}} \int_{-\sqrt{R^2-b^2-x^2}}^{\sqrt{R^2-b^2-x^2}} \frac{R}{\sqrt{R^2-x^2-y^2}} dy dx,
 \end{aligned} \tag{8}$$

where the impact parameter  $b$  spans the range  $(0, R)$  and  $D$  is a projection of the sphere on the OXY plane.

The second geometrical situation we wish to consider corresponds to two spheres that penetrate each other (hereafter 'sphere-sphere'). Hence, the final shape looks as a sphere without a double spherical dome like *e.g.* a lens. Assuming that the two nuclei are identical, the surface of the spectator prefragment will be similar to that of the initial sphere, but its volume will be different.

The third geometrical situation considered in this work takes, in an effective way, into account the dynamics of the process. It is based on the idea that the collision is very fast, and the nuclei interact with each other as a finite-size bullet grazing a sphere, or said differently, the projectile scraps the target with a cylinder (hereafter 'sphere-cylinder'). The shape obtained under this assumption is rather exotic, complex to calculate geometrically; though it seems to be most realistic for the beam energies typical at the CERN SPS [12].

The equations governing the calculation of the aforementioned three geometrical configurations, and namely the surface, are detailed in Appendix A. Figure 1 presents the dependence of the mass of the spectator prefragment on the impact parameter in the  $^{208}\text{Pb}+^{208}\text{Pb}$  collisions for the three scenarios. Since, for a given impact parameter, the corresponding shapes have distinct volumes, the remnant mass obtained in the three cases is different, as well as its surface, neutron and proton numbers.

We note that, under the assumption that the nucleus equilibrates its shape from deformed to spherical quickly compared to the time of its decay, we neglect the explicit

treatment of the dynamics of this first shape relaxation process. That is, for each impact parameter, the resulting prefragment mass, charge and excitation energy are calculated based on geometrical considerations only, as detailed below.

Once the shape of the spectator prefragment is established for a given scenario and impact parameter, a purely macroscopic picture is proposed in this work in order to determine its excitation energy. It is assumed that a sound estimate of the latter can be obtained from the deformation energy as predicted by the LDM within the sudden cut-off approximation. The Lublin-Strasbourg Drop (LSD) model [13, 14] is used in this study. The main contribution to the deformation energy of a nucleus is given by the surface energy; the Coulomb and curvature energies giving second-order corrections. In this work, we therefore approximate the prefragment deformation energy with its surface energy. For a deformed nucleus with mass  $A$  and charge  $Z$ , the LDM surface energy reads:

$$E_{\text{surf.}}(A, Z; def) = b_{\text{surf.}} (1 - \kappa_{\text{surf.}} I^2) A^{2/3} B_{\text{surf.}}(def). \tag{9}$$

where  $I = (A - 2Z)/A$ . The deformation-dependent term is defined as the surface energy of the deformed body normalized to that of a sphere of the same volume:

$$B_{\text{surf.}}(def) = \frac{S(def)}{S(sphere)}. \tag{10}$$

Details about the LDM formulas, and its LSD implementation and parameters can be found in Appendix B.

As introduced in this section, in the proposed simple geometrical macroscopic abrasion model, the excitation energy would be given by Eq. 1 where  $E_{LDM}$  is approximated by  $E_{\text{surf}}$  in the LSD parameterization. According to [15] the excitation energy derived from the surface-energy excess of the deformed prefragment is too low. Guided by the results of [16], in the present work, the excitation energy considered in the framework of the purely geometrical macroscopic approach is taken as *two times* the value calculated with Eq. 1.

Figure 2 shows the excitation energy predicted by the macroscopic approach for the three considered geometrical scenarios, as a function of impact parameter (a), and spectator mass (b). It is observed that, depending on the geometrical abrasion hypothesis, the excitation energy can have a rather different behavior, and take substantially different values<sup>1</sup>. The largest excitation energy is predicted for close-to-central collisions in the 'sphere-sphere' picture, since the spectator object after

<sup>1</sup> Preliminary results reported in [17] suffered from some technical issue, yielding somewhat erroneous numerical values. Yet, the issue, solved here, did not affect the main outcome and conclusion of that work.

the collision has the most curved and deformed shape. The excitation energy expected within this model can reach up to 500 MeV, where multifragmentation-like processes are very likely to contribute. The 'sphere-plane' and 'sphere-cylinder' scenarios predict excitation energies below about 100 MeV and 150 MeV, respectively, for semi-central collisions. This  $E^*$  regime is within the domain of applicability of the stochastic Langevin approach restricted to the competition between evaporation and fission.

The correlation between prefragment mass and excitation energy is crucial in the calculation of its time evolution and decay. Note that, within the here-proposed simplest geometrical macroscopic picture, the correspondence between excitation energy and impact parameter (equivalently, mass) is a *one-to-one* correspondence. Furthermore, the angular momentum of the spectator prefragment is assumed to be negligible; this approximation is reasonable for the present exploratory study, and can be easily leveled-off in future. The black crosses in Fig. 2 mark the prefragments which were selected for further investigation of the geometrical macroscopic picture and combined to the dynamical Langevin approach. The 'sphere-cylinder' scenario is chosen for this investigation, as it seems the most realistic assumption. The arrow at  $b \approx 10$  fm in Fig. 2 a) indicates the impact parameter considered in [2] for studying the influence of the spectator electromagnetic field on pions.

We note that the predicted value of the prefragment excitation energy can also be influenced by the specific LDM parameterization used. This is illustrated in Fig. 3 which displays the correspondence between prefragment mass and excitation energy for the 'sphere-cylinder' scenario, as obtained with most popular implementations of the LDM. The largest excitation energies are predicted by the Finite Range Liquid Drop Model with the latest set of parameters (FRLDM, 2004 [20]), while the lowest excitation energies are obtained with Moretto's prescription (Moretto, 2012 [21]). The LSD model used in this work predicts values close to the lower boundary, hardly exceeding 100 MeV. The spread in excitation energy depending on the LDM used can reach 40 MeV. That shall give an idea about the uncertainty range of the spectator excitation energy predicted within the geometrical macroscopic abrasion model proposed in this work.

## B. Statistical abrasion model of Gaimard-Schmidt

The geometrical picture sketched above is also the basis of the abrasion model (ABRA) of Gaimard-Schmidt [8] widely used in the field. For a given abraded mass, the protons and neutrons are assumed to be removed randomly from the projectile, and statistical fluctuations given by the hyper-geometrical distribution yield the neutron-to-proton ratio of the prefragment spectator.

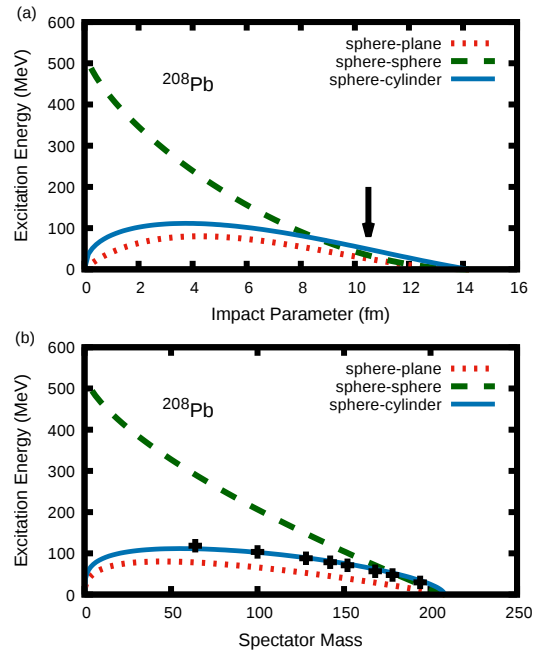


FIG. 2: (Color on-line) Dependence of the prefragment excitation energy for the three geometrical scenarios described in the text, on impact parameter (a), and on mass (b). The arrow indicates the impact parameter considered in [2]. Crosses in panel (b) mark the nuclei selected as typical examples for further dynamical calculations.

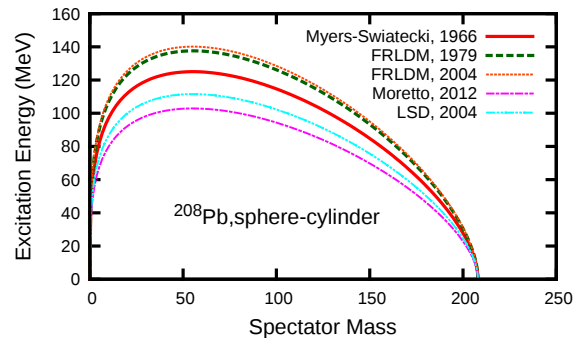


FIG. 3: (Color on-line) Dependence of the spectator prefragment excitation energy on its mass for various LDM realizations: Myers-Swiatecki, 1966 [18], FRLDM, 1979 [19], FRLDM, 2004 [20], Moretto, 2012 [21], and LSD, 2004 [13].

A major difference as compared to the picture outlined in the previous section is that the calculation of the prefragment excitation energy implemented in the ABRA code is not based on a geometrical macroscopic approach. Rather, it is given by the energy of the vacancies created in the single-particle (s.p.) levels with respect to the Fermi surface [16]. In this sense, ABRA accounts for microscopic effects in the entrance channel of the reaction, contrary to the macroscopic picture of

the previous section. The excitation energy computed this way leads to higher values than those based on the surface energy excess [8]. Though, comparison with experiment suggests that the calculation based on s.p. levels vacancies still gives a too low excitation energy. The result was thus further empirically adjusted by multiplying the theoretical value by a factor of two [16]. This is what is implemented in ABRA. The deviation between the theoretical calculation and the empirically adjusted value may be due to friction effects or final-state interactions [8, 15, 16]. The angular momentum of the prefragment in ABRA is calculated as the sum of the angular momenta of the nucleons removed in the collision [22].

To describe the entire reaction, from the early collision up to the final cold products are reached, the ABRA code is usually combined with the statistical evaporation model ABLA [9]. In its most general form, the ABRABLA code consists of three stages: (1) abrasion (ABRA), (2) if the temperature of the remnant after abrasion is above a limiting value (around 4.5 MeV), the system breaks up in several more or less heavy intermediate products [23], (3) de-excitation (ABLA) of the heavy remnants from stage (1) or (1)+(2). We note that in the first stage of the reaction, the code considers that abrasion can be induced by, either nuclear or electromagnetic, interactions. The latter are confined to large impact parameters, and their probability increases with the charge of the colliding ions. They involve small, below about 30 MeV, excitation energy. We finally emphasize that ABRABLA computes the decay of the heavy-ion remnant of the collision, only. The decay of the nuclear matter in the overlapping zone is not followed.

In the remainder of this work, unless explicitly specified, we consider only those events from ABRABLA which do not pass by stage (2); that is, the very-highly excited prefragments experiencing a break-up process prior 'standard' de-excitation are excluded. Events with IMF emission are not considered neither, as well as we do overlook electromagnetic-induced reactions. All in all, we restrict to those events which undergo most 'standard' low-energy de-excitation process, leading to, either evaporation of light particles and formation of a heavy evaporation residue (ER), or fission possibly accompanied by light-particle emission. This restriction is chosen in order to permit most meaningful comparison with the Langevin calculations detailed later below, and which model the ER and fission channels, only. We emphasize that this selection excludes very central collisions. That is welcome also, since the geometrical abrasion picture outlined above makes certainly most sense for the more peripheral collisions. Finally, the study of Ref. [2] about the influence of spectator-induced electromagnetic fields on pion trajectories was done for  $b \approx 10.5$  fm, belonging to the peripheral collision domain.

Figure 4 shows the correlation between the prefragment excitation energy and mass (a), and the prefragment excitation energy and impact parameter (b) as pre-

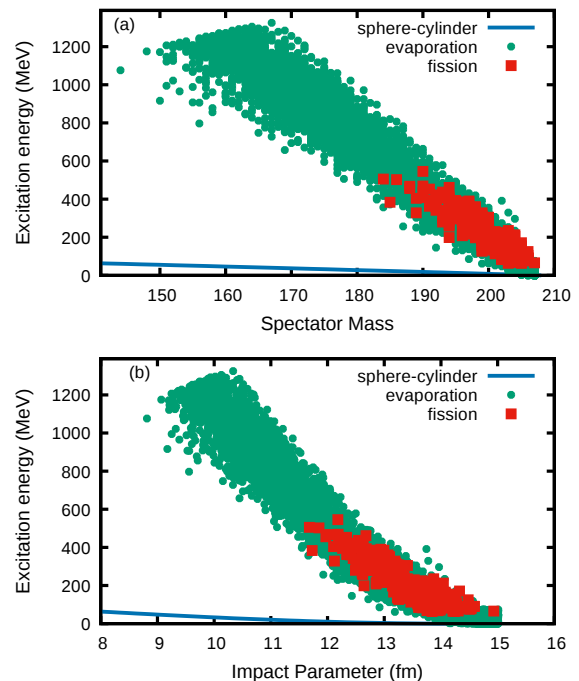


FIG. 4: (Color on-line) Correlation between the prefragment excitation energy on its mass (a), and on impact parameter (b) for events ending with the formation of a single heavy ER, or with fission, as predicted by the ABRABLA code. For comparison, the correlation computed in the geometrical macroscopic model for the 'sphere-cylinder' is shown again.

dicted with ABRABLA. Events ending in fission or the survival of a single heavy evaporation residue are shown separately. The full line displays again the dependence of the excitation energy on mass and impact parameter, respectively, as determined with the geometrical 'sphere-cylinder' picture in the previous section. It is clear that ABRA gives much higher excitation energies than the geometrical macroscopic calculation, as shown already in Ref. [8]. The geometrical calculation extends down to the lowest prefragment masses (see also Fig. 2b), while such events are not present for ABRA as they usually imply passage through the break-up stage (2) which we disregard.

In the present work, in addition to analyzing the predictions of the ABRABLA code as such, we also construct a 'hybrid' model, by using the results of ABRA as an input for the dynamical calculations within the Langevin approach presented below. That will permit to investigate the influence of i) the modeling of the prefragment properties in the abrasion stage, and ii) the difference between the de-excitation path based on a statistical or dynamical model.

The ABRABLA code has shown successful over a wide beam energy range from about 100 to several thousands of MeV/nucleon. To our knowledge, it was never tested in the ultra-relativistic energy domain of this work. As

mentioned above, the ABRA stage may implicitly imply some degree of friction between the colliding nuclei. Whether friction is still present at ultra-relativistic velocities is not obvious. Hence, any attempt to probe the upper energy limit for the validity of the ideas behind ABRA is worthy consideration. The exploratory work done here suggests these ideas to be rather robust, as will be seen further below.

### C. Microscopic Glauber abrasion model

At relativistic beam energy, the abrasion cross section is most often computed, like in the two previous sections, assuming a geometrical picture for the impact parameter distribution. A more elaborate prescription was proposed with the Glauber theory of multiple scattering [11]. The Glauber model is a microscopic approach which uses the matter densities calculated for protons and neutrons removed from the nucleus. The nuclear matter densities are obtained from the Woods-Saxon potential, or any other s.p. potential. In the present work, the Hartree-Fock-Bogolyubov (HFB) method is used assuming a spherical shape for  $^{208}\text{Pb}$  [24].

The abrasion cross section from the Glauber model has the form:

$$\sigma_{abr}^i(N) = \binom{A}{N} 2\pi \int_0^{b_{max}} b db (1 - P_i(b))^N (P_i(b))^{A_i - N}, \quad (11)$$

where  $A_i$  is the mass number of one of the colliding nuclei (indexed  $i, j$ ),  $N$  is the number of abraded nucleons and

$$P_i(\vec{b}) = \int d^2\vec{s} D_i(\vec{s}) \exp(-A_j \sigma_{NN} D_j(\vec{s} + \vec{b})) \quad (12)$$

with  $i, j = 1, 2$  and  $i \neq j$ . The density function of the colliding nuclei is

$$D_i(\vec{s}) = \int_{-\infty}^{\infty} dz \rho_i(\vec{s}, z). \quad (13)$$

We take  $\sigma_{NN}=40$  mb for practical calculations, and the HFB neutron/proton densities are used to calculate  $D(\vec{s})$  and  $P(\vec{b})$ .

In Fig. 5 the impact parameter distribution (equivalently, abrasion cross section) as predicted by the Glauber model is compared to the purely geometrical picture. Up to  $b=10$  fm the Glauber distribution coincides with the latter, before it drops to zero at higher impact parameters.

As for the prefragment excitation energy, in our implementation of the Glauber model, either the Gaimard-Schmidt [8, 16], or the Ericson [25] approach can be used. Depending on this choice, the mean excitation energy imparted to the remnant ranges from 10 to 20 MeV per abraded nucleon. The excitation energy in our Glauber model is then taken as:

$$E_{exc} = N\Delta E, \quad (14)$$

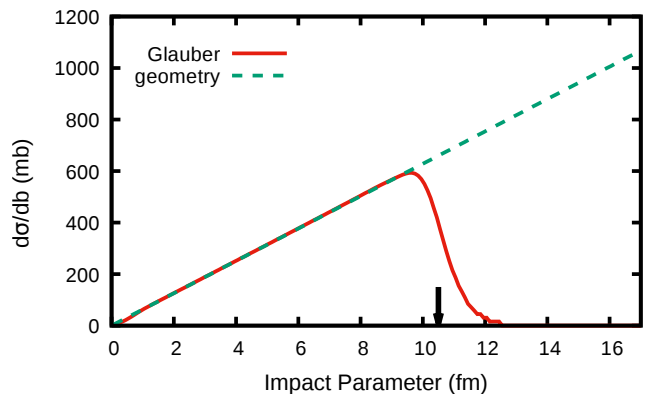


FIG. 5: (Color on-line) Impact parameter distribution obtained from the Glauber formula (Eq. 11) and from the geometrical prescription. The arrow marks the  $b$  value studied in [2].

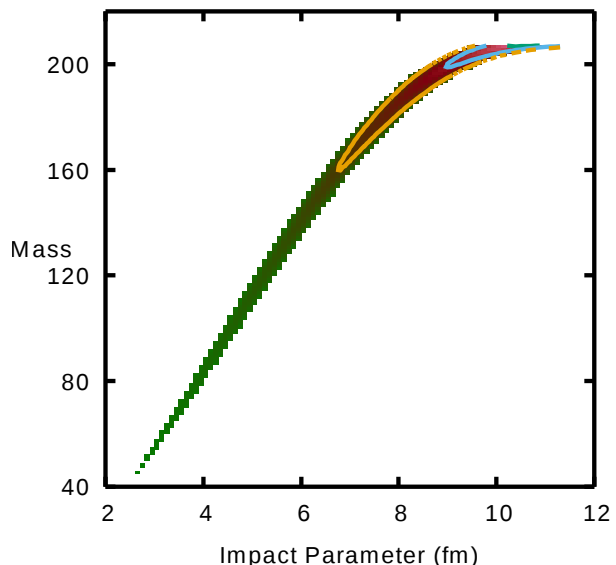


FIG. 6: (Color on-line) Correlation between the spectator mass and impact parameter of the collision as obtained from the Glauber formula (Eq. 11).

where  $N$  is the number of abraded nucleons, which makes sense provided that  $N \ll A$ , *i.e.* the number of holes is small, as it is the case in peripheral collisions. For practical calculations we consider  $\Delta E = 10$  MeV. The correlation between the prefragment excitation energy and its mass is displayed in Fig. 6. When compared to the geometrical (Fig. 1) and ABRA (Fig. 4) results, our implementation of the Glauber approach yields a less steep decrease of prefragment mass with decreasing impact parameter, and leads to lower excitation energies.

### III. DYNAMICAL DECAY OF THE SPECTATOR PREFRAGMENT

To describe the decay of the hot remnant formed in the abrasion stage, a statistical model is most commonly used. In the present work, we propose to innovatively extended the description of the second (ablation) stage with a dynamical model.

The time evolution of the fissioning nucleus is described within the stochastic approach [26–28]. Most relevant degrees of freedom are introduced as collective coordinates, and their evolution with time is treated as the motion of Brownian particles, which interact stochastically with the larger number of internal degrees of freedom constituting a surrounding ‘heat bath’. The details of the approach can be found in [29], and references therein; only the main features are given below.

In the present implementation of the stochastic method, four collective coordinates are considered. Three out of them define the shape of the nucleus, while the fourth defines its orientation in space. The coordinates  $\mathbf{q} = (q_1, q_2, q_3)$  are connected to, respectively, elongation, neck thickness and left-right asymmetry [30, 31]. They are based on the popular Funny-Hills  $(c, h, \alpha)$  nuclear-shape parameterization [32]. The collective coordinate  $q_4 = K$  is taken as the projection of the angular momentum  $L$  of the nucleus onto the fission axis, varying in the range  $(-L, +L)$ . In the present work, whenever the dynamical stage is combined with the geometrical macroscopic or the Glauber abrasion models, the angular momentum imparted to the heavy remnant is not evaluated, and  $L$  is set to zero in first approximation. The dynamical calculation is hence three-dimensional, only. On the contrary, when the dynamical stage is fed with the input from the ABRA abrasion model, the angular momentum is directly taken from ABRA. The second stage is then effectively a four-dimensional calculation.<sup>2</sup> Within the present stochastic approach, the time evolution of the shape coordinates is given by the solution of the Langevin equation:

$$\begin{aligned} \frac{dq_i}{dt} &= \sum_j \mu_{ij}(\vec{q}) p_j, \\ \frac{dp_i}{dt} &= -\frac{1}{2} \sum_{j,k} \frac{d\mu_{ij}(\vec{q})}{dq_i} p_j p_k - \frac{dF(\vec{q})}{dq_i} \\ &\quad - \sum_{j,k} \gamma_{ij}(\vec{q}) \mu_{ij}(\vec{q}) p_k + \sum_j \theta_{ij}(\vec{q}) \xi_j(t), \end{aligned} \quad (15)$$

for  $\mathbf{q}$  the vector of collective coordinates, and  $\mathbf{p}$  the vector of conjugate momenta. The evolution is governed

by driving potential, friction and inertia forces, all explicit functions of deformation. A similar equation, with some variation to take the specificity of this model into account, holds for  $q_4 = K$  [29].

The driving potential is given by the  $F(\mathbf{q}) = V(\mathbf{q}) - a(\mathbf{q})T^2$  Helmholtz free energy, where the bare potential energy  $V(\mathbf{q})$  is obtained from the LSD model, and  $T$  is the temperature of the decaying system. The inertia tensor  $m_{ij}(\mathbf{q})$  is calculated under the Werner-Wheeler approximation of an incompressible irrotational flow [33]. The friction tensor  $\gamma_{ij}(\mathbf{q})$  is derived from the one-body *wall-plus-window* prescription [34] modified in order to account properly for chaoticity of the nucleon movement inside the deformed nucleus [35]. Fluctuations are modeled by the random force  $\theta_{ij}$  related to friction by the Einstein relation  $\sum \theta_{ik} \theta_{kj} = T \gamma_{ij}$ . The temperature of the system  $T$  is determined by the Fermi-gas model formula

$$T = (E_{\text{int}}/a)^{1/2}, \quad (16)$$

where  $E_{\text{int}}$  is the internal excitation energy of the nucleus, and  $a$  is the level-density parameter.

Along its dynamical evolution the system may evaporate particles and  $\gamma$ -rays. The Master equation governing this process is coupled to the multi-dimensional Langevin equation [36]. Both set of equations are solved together within a Monte Carlo framework [30] time-step by time-step ( $\Delta t = 10^{-23}$ s). At each step, the properties of the decaying system (in mass, charge, excitation energy, and angular momentum wherever applicable) are recalculated taking into account its possible change of shape, or evaporation of a particle. If the nucleus, along its trajectory, is driven to a very elongated and necked-in shape, it splits into two fragments, *i.e.* fission occurs. Any particle emitted before this so-called scission point is then denominated ‘pre-scission’ particle. On the contrary, if the nucleus exhausts its excitation energy before reaching a scission shape, it ends in the state of a heavy evaporation residue (ER).

Figure 7 shows the fission barrier of some specific heavy nuclei as a function of their left-right shape asymmetry and their temperature. The  $T$ -dependent barrier is defined as the difference between the free energy at the saddle point and at the equilibrium ground state. It represents the energy the nucleus has to possess in order to have a chance (classically) to fission. This threshold energy clearly depends on the how the nucleus splits *i.e.* in fragments of either equal or different size. For example, the topography of the maps in Fig. 7 suggests that  $^{100}\text{Y}$  will most likely fission into asymmetric fragments independent of the temperature (as the barrier to overcome is lower for  $q_3$  non zero), while the heavier systems of the figure will most often experience symmetric fission. We note also that increasing temperature usually induces broader fragment mass (equivalently, charge) distributions, as suggested by the softer driving potential landscapes in the  $q_3$  asymmetry direction when  $T$  is larger, as well as

<sup>2</sup> The difference in angular-momentum treatment depending on the abrasion model has no significant influence on the observables of our study, as the angular momentum imparted to the heavy prefragment remains limited to a few  $\hbar$  on average [8].

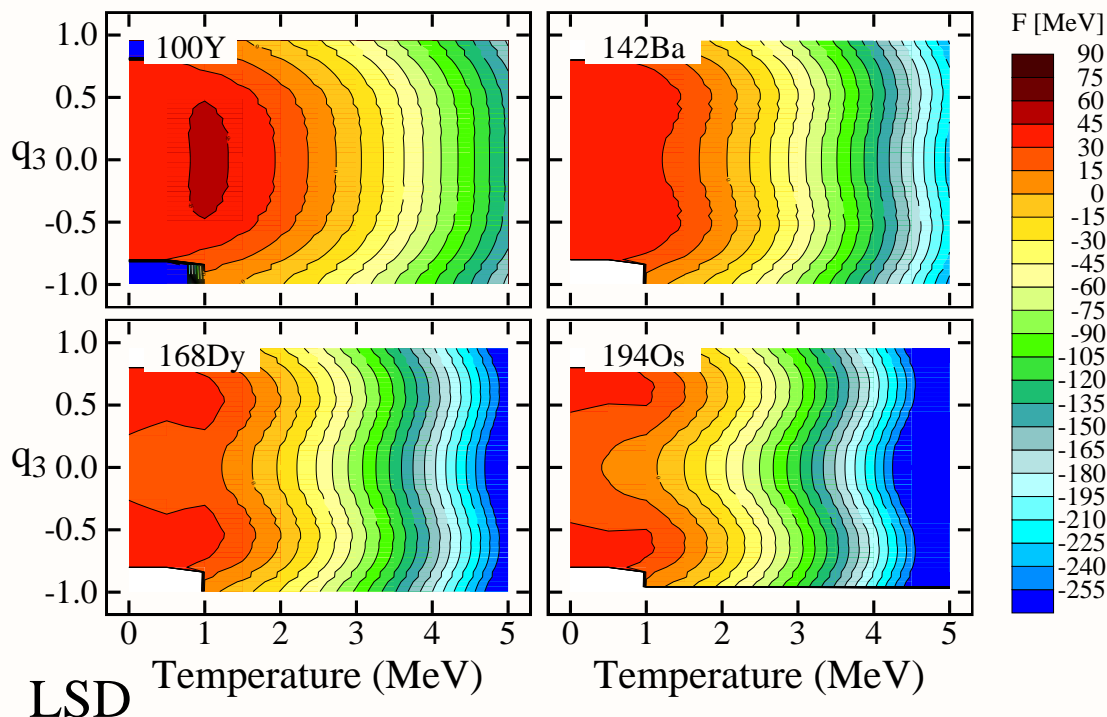


FIG. 7: Fission barrier in the  $(T, q_3)$  plane for a sample of nuclei. Here the barrier is defined as the difference between the free energy at the conditional ( $q_3$ -constrained) saddle point and the ground-state equilibrium point. The landscapes are presented for  $^{100}\text{Y}$ ,  $^{142}\text{Ba}$ ,  $^{168}\text{Dy}$  and  $^{194}\text{Os}$ .

due to larger fluctuations.

The dynamical approach is aimed to model the second stage of the collision. In the present work, it is combined to the three abrasion models of Section II, leading to three different reaction softwares, called LSD-Lang, Glauber-Lang, and ABRA-Lang, respectively. For sake of comparison, calculations with the ABRABLA code will be presented as well, in which the ABRA abrasion model is combined to its companion decayl model ABLA. The latter has shown very powerful in describing the competition between the various open decay channels (evaporation and fission for the concern of this work), as well as the properties (mass, charge, energy) of the light-particle and heavy residue or fission fragment products. As compared to other statistical models, ABLA possesses some specific assets. These comprise a parameterization of the fission-decay width which accounts to some extent and in an effective way for friction effects along the path to fission, and the explicitly account of an elaborate empirical potential landscape for the determination of fission fragment properties [9]. Though, like any statistical model,

the ABLA software does not give a direct access to a true time for the decay.

## IV. RESULTS

### A. Geometrical macroscopic abrasion coupled to dynamical decay

As noted in Section II A, in the geometrical macroscopic picture, there is a one-to-one correspondence between impact parameter, spectator mass and charge, and excitation energy ( $A, Z, E^*$ ). In the present work, for the LSD-Lang combination, we consider a few prefragments, only. It is hoped that the restriction to some cases permits to better understand which region of the initial  $(A, Z, E^*)$  phase space contributes to a specific region of the populated final products. The selected nuclei are marked with black crosses in Fig. 2:  $^{194}\text{Os}$ ,  $^{181}\text{Lu}$ ,  $^{168}\text{Dy}$ ,  $^{152}\text{Nd}$ ,  $^{142}\text{Ba}$ ,  $^{128}\text{Sn}$ ,  $^{100}\text{Y}$ , and  $^{64}\text{Mn}$ , formed in collisions with impact parameter decreasing from around 12 to 4 fm. The initial excitation energy is below 150

MeV ('sphere-cylinder' scenario), increasing roughly linearly with increasing abraded mass, see Fig. 2 (b).

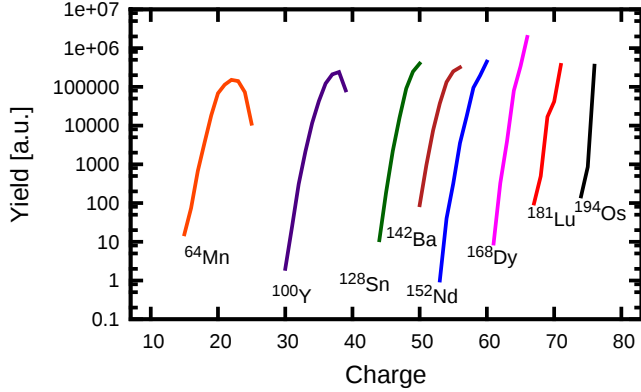


FIG. 8: (Color on-line) Charge distribution of the evaporation residues produced along the decay of the set of prefragments selected for the LSD-Lang calculation. The spectator is specified next to each curve. The integral of each distribution was scaled according to the probability that the decay ends in the ER channel.

Figure 8 presents the charge distribution of the ERs produced along the decay of the considered prefragments. The integral under the curves reflects the ER channel probability; it decreases with increasing abraded mass due to the increasing excitation energy and thus enhanced fission probability. However, the magnitude of the difference is very small, since ER decay largely dominates (see further below). Note that weighting by the impact parameter distribution is not included at this step. With increasing abraded mass, the maximum of the ER distribution is observed to shift away from the charge of the prefragment, leading to a progressive change in the shape of the distribution. This is, of course, due to the increased probability of charged-particle evaporation with increasing prefragment  $E^*$  and, to lesser extent, decreasing mass.

The charge distribution populated in the fission channel (complementary to ER) is shown in Fig. 9, again for the sample of selected prefragments. Note that, here, the presented yields do not reflect the fission probability; curves were arbitrarily displaced vertically for clarity. While fission of the heaviest prefragments is symmetric (centered around about half the charge of the prefragment), the fission partition becomes progressively asymmetric (the two fragments are not of equal charge) with increasing abraded mass. The shape of the distributions roughly reflect the topography of the energy landscapes presented in Fig. 7: for  $^{100}\text{Y}$  with a mean temperature at scission  $\langle T_{sc} \rangle = 2.91$  MeV,  $^{142}\text{Ba}$  with  $\langle T_{sc} \rangle = 2.18$  MeV,  $^{168}\text{Dy}$  with  $\langle T_{sc} \rangle = 1.73$  MeV, and  $^{194}\text{Os}$  with  $\langle T_{sc} \rangle = 1.17$  MeV. The lower the energy, the more favored the corresponding  $q_3$  partition. This change in the shape of the fragment charge (equivalently, mass) distribution illustrates the

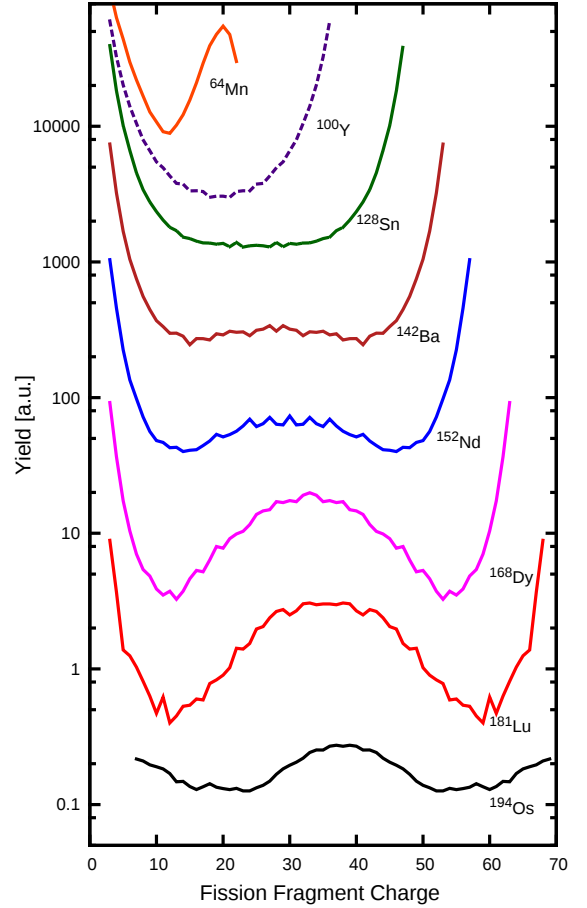


FIG. 9: (Color on-line) Charge distribution of the fission fragments produced along the decay of the set of prefragments selected for the LSD-Lang calculation. The spectator is specified next to each curve. The integral of the curves do not reflect the fission probabilities (which are given in Table I); curves were displaced arbitrarily in the vertical direction for better legibility.

signature of the Businaro-Gallone (BG) transition, located between Sn and Ba in the present temperature regime [37] for the LSD model.

A summary of the properties of the prefragment decay is given in Fig. 10: the fission probability and number of particles ( $n$ ,  $p$ ,  $\alpha$ ,  $d$ ,  $t$ ) emitted along the decay in the ER and fission channels are displayed as a function of spectator mass. The increase of the fission probability with increasing abraded mass is due to the corresponding increase in prefragment excitation energy. Though, it is to be noted that the fission probability remains small in all cases (below a few %) due to the low fissility of nuclei situated below Pb. Independent of the decay channel (ER or fission) the multiplicities of the emitted particles also increases from  $^{194}\text{Os}$  to  $^{64}\text{Mn}$ , reflecting again the increasing excitation of the product left after abrasion. The variation of the neutron multiplicity (panel b) tends

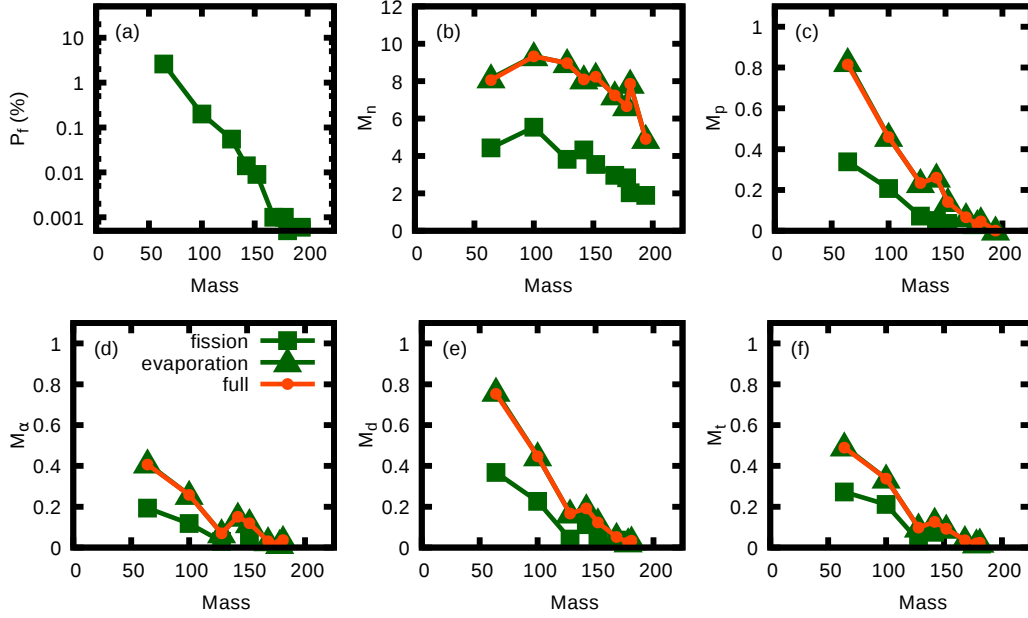


FIG. 10: (Color on-line) Fission probability and mean multiplicities of neutrons, protons,  $\alpha$  particles, deuterons and tritons emitted along the deexcitation of the excited spectator on its way to either formation of an evaporation residue (green triangles), or fission (green squares). The average multiplicities, irrespective of the decay channel, are shown also (orange dots).

though to develop a plateau with decreasing spectator mass. This is related to the increasing competition of charged-particle emission (panels c to f) for higher excitation and lighter systems, and which takes away a part of the energy available for neutron evaporation. Finally, it is observed that more particles (of any kind) are emitted in the ER channel than in the fission channel. The reason behind this difference is the energy required by the system to overcome the (large) fission barrier, which energy is then not available any more for evaporation.

We show also in Fig. 10 the average multiplicities independent of the decay channel. They are, of course, very close to those obtained when selecting the ER channel, since the latter widely dominates. It is customary in theoretical work in the low energy domain (below about 10 MeV/nucleon) to analyze the ER and fission channels separately, since they are usually tagged in experiment. However, in studies at ultra-relativistic energies, experimental information about the decay of the spectator is very scarce as discussed above. In addition, according to the high velocity-boost of the projectile, all products (heavy and light) are strongly forward focused and moving fast. Discriminating particles from the ER and fission channels is therefore very difficult, and was not attempted yet to our knowledge. Hence, it is the average multiplicity, irrespective of the fate of the spectator, that is most useful for comparison with experiment on particle multiplicities wherever available.

### B. Gaimard-Schmidt abrasion coupled to dynamical decay and comparison with ABRABLA

As noted earlier, the output of the abrasion model based of Refs. [8, 16], in terms of prefragment mass, charge, excitation energy and angular momentum, is used as input for the dynamical code, and is referred to as ABLA-Lang. Combining the predictions by the LSD-Lang and ABRA-Lang softwares will permit to shed light on the influence of the first stage of the reaction. The predictions are further compared to the results of the ABRABLA code, yielding information, in this case, about the second stage.

The outcome of ABRA-Lang and ABRABLA is gathered in Fig. 11 for the charge distribution for which experimental data exist for [38, 39] for the  $^{208}\text{Pb}$  (158 GeV/nucleon) +  $^{208}\text{Pb}$  collision. Figures 11 (a) and (b) restrict, respectively, to the ER and fission channel, while (c) includes both channels. Note that, since ABRA-Lang uses the input file produced by ABRA, it automatically considers the same impact parameter distribution as ABRABLA. The ER charge is observed to extend to much smaller values in ABRABLA as compared to ABRA-Lang. On the contrary, the fission-fragment charge distribution scans a wider domain for ABRA-Lang than for ABRABLA. The fission-fragment charge distribution is Gaussian-like and well localized for ABRABLA, suggesting that fission is mainly populated by the decay of heavy prefragments with  $Z$  from about 60 to 80. The heaviest, lowly excited, and lightest, very excited, prefragments experience, respectively, very short

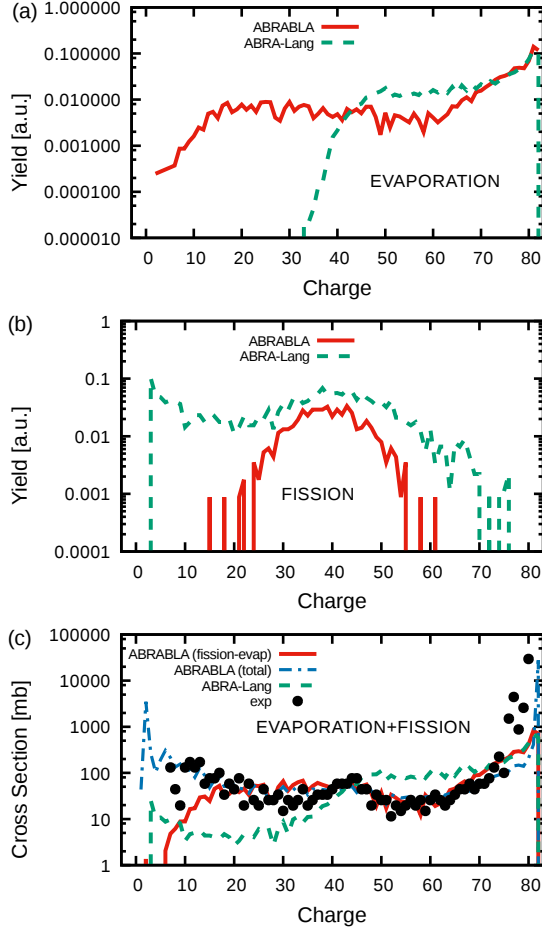


FIG. 11: (Color on-line) Charge distribution of the evaporation residues (a) and fission fragments (b) obtained with the ABRA-Lang (dashed line) and ABRABLA (full line) codes. Weighting by the impact parameter distribution predicted by ABRA is performed in both cases. The integral distributions including ER and fission channels are shown in (c); normalization to absolute cross sections is performed using the nuclear-induced reaction cross section extracted in experiment [38]. The total distribution predicted by the ABRABLA code, with no event selection (that is, including electromagnetic-induced interactions, and break-up processes) is displayed as well with the dash-dotted curve; absolute normalization is directly taken from the total reaction cross section predicted by ABRABLA. Experimental data are from Refs. [38, 39].

and long evaporation cascades. On the other hand, in ABRA-Lang, the light prefragments at the high excitation predicted by ABRA undergo fission. This explains the non-symmetric shape of the ABRA-Lang distribution in Fig. 11 (b) which results from the convolution of the individual distributions of Fig. 9.

The comparison between various observables commonly investigated in the field is given in Table I. The average fission probability presented in Table I shows indeed a huge increase between LSD-Lang and ABRA-

TABLE I: ER and fission observables as predicted by the LSD-Lang ('sphere-cylinder' scenario), ABRA-Lang and ABRABLA codes for  $^{208}\text{Pb}$  (158 GeV/nucleon) +  $^{208}\text{Pb}$ . All calculations use the impact parameter distribution predicted by ABRA, and averaging is performed over all products in the ER (respectively, fission) channel. The listed quantities correspond to the fission probability  $P_f$ , number of light particles emitted in each channel: multiplicities of pre-scission neutrons, protons and  $\alpha$ 's ( $n_{pre}$ ,  $p_{pre}$ ,  $\alpha_{pre}$ ), and of the particles leading to a cold ER ( $n_{ER}$ ,  $p_{ER}$ ,  $\alpha_{ER}$ ). The fission time  $t_f$  is given also.

	LSD-Lang	ABRA-Lang
$P_f$	0.00014	0.01879
$n_{pre}$	3.0035	15.0651
$n_{ER}$	6.9075	16.264
$p_{pre}$	0.0208	2.586
$p_{ER}$	0.0953	1.9427
$\alpha_{pre}$	0.0099	0.590
$\alpha_{ER}$	0.0530	0.572
$t_f, 10^{-21}\text{s}$	11.272	14.636

Lang, due to the larger prefragment spectator excitation. These observations shows that the Langevin code predicts more fission in light systems, than the statistical ABLA model. One reason for explaining this difference may be the parameterization of the empirical potential used in ABLA, adjusted to fission of heavy nuclei, and which may not be best-suited any more around and below the BG transition. Another reason of the difference may be related to dissipation effects. Elucidating the intricate interplay of these (and others) possible reasons is beyond the scope of this work.

The substantial difference between the light-particle multiplicities predicted by LSD-Lang and ABRA-Lang directly reflects the difference in initial excitation energy as depending on the abrasion model. A larger fission time for ABRA-Lang is connected to the time required to emit more particles before fission. It is not easy to trace back at this stage, as it additionally includes an averaging over prefragments with different yields in each channel, depending on the model, as discussed above around Fig. 11 (b).

Finally, in Fig. 11 (c) we display the sum of the ER and fission channels as predicted by ABRA-Lang and ABRABLA. Normalization to absolute cross sections is performed with the nuclear-induced reaction cross section extracted in experiment [38]. The rather remarkable description of the shape of the experimental distribution with ABRABLA (red full line) in the region where the ER and fission dominate is noteworthy. The description by ABRA-Lang (green dashed line) is very encouraging,

having in mind its dynamical framework, which is confronted to such kind of data in a 'brute-force' manner here for the first time.

We overlay also in Fig. 11 (c) the prediction by the ABRABLA code (blue dash-dotted line), including all types of interactions (nuclear- and electromagnetic-induced), all kinds of decay channels (ER, fission, with or without break-up, IMF emission), and normalized with the ABRABLA-predicted total reaction cross section. Inclusion of electromagnetic-induced reactions improves the description close to the projectile mass, as expected, while break-up and IMF contribute to enhance the yields of lighter products. The overall description of ABRABLA is very good. So far, the achievement of the code was studied in detail and demonstrated powerful at relativistic beam energy. To our knowledge, this is the first time that it is tested at ultra-relativistic energy, showing good extrapolation property.

### C. Reaction time scales and possible connection with pion electromagnetic effects

In Ref. [2] it is proposed that the distortion observed in the positively- and negatively-charged pion spectra is caused by the electromagnetic field generated by the heavy spectators moving at relativistic velocity, provided that these live long enough. In this context, one of the main assets of dynamical calculations used in this work is the possibility to predict the decay time of the excited spectator, including the time scale (and sequence) of the light particles emitted along its decay, i.e. the time taken to either reach a cold ER or to fission into two fragments.

As noted earlier, the main decay channel of the excited spectators formed in lead on lead collisions is found to be the formation of a heavy residue. From Table I we see that the corresponding events are characterized by emission of neutrons mainly<sup>3</sup>). That is, the collision leads to two highly-charged residues, in the vicinity of the pions produced by fireball or from fire-streak at the SPS energies. These residues live long enough to interact electromagnetically with pions. For the remaining events, *i.e.* when fission occurs, much smaller product charges are reached. That can reduce electromagnetic effects on pions, except when the system lives long-enough before splitting into two parts. The Langevin approach is particularly suited to investigate the fission time scale. In Fig. 12 the mean fission time is displayed as a function of prefragment mass in the rest frame of the spectator system<sup>4</sup>, as obtained with

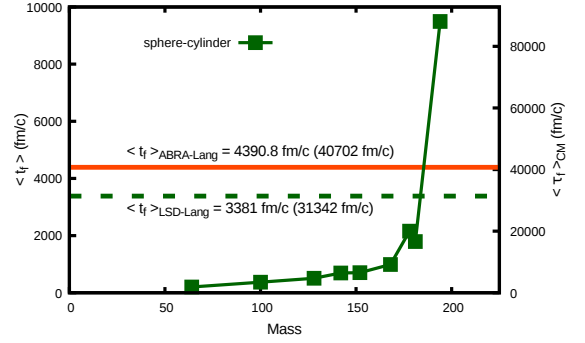


FIG. 12: Mean fission time as a function of spectator mass in the LSD-Lang code. The right-side  $y$ -axis gives the time as output from the Langevin calculation, in the fission frame, and which is transformed to the overall center-of-mass time on the left-side  $y$ -axis. Horizontal lines indicate the mean fission time averaged over all spectators for the LSD-Lang (green dashed) and ABRA-Lang (orange full) codes.

the LSD-Lang code ('sphere-cylinder' scenario). Longer times for the heavier prefragments are due to the smaller excitation energy in peripheral collisions. Also given is the mean time averaged over all spectators (horizontal lines) as obtained with the LSD-Lang and ABRA-Lang ( $\langle t_f \rangle_{\text{LSD-Lang}}$  and  $\langle t_f \rangle_{\text{ABRA-Lang}}$ , respectively). The predicted fission time in the rest-frame of the spectator is in the range 50-3000 fm/c, and even longer for very peripheral collisions. After Lorentz transformation, this yields an overall center-of-mass time  $\tau_{\text{CM}}$  of the colliding nuclei which is enough to guarantee long-lasting electromagnetic interactions between the spectators and the pions ejected from the quark-gluon plasma. In the numerical simulations of the electromagnetic effects the trajectories are followed till  $\tau_{\text{CM}} \sim 1000$  fm/c.

The time measured in the spectator reference frame can be transformed to the overall center-of-mass system (right  $y$ -scale in Fig. 12) as:

$$\tau_{\text{CM}} = \frac{t_{\text{spec}}}{\sqrt{1 - \beta_{\text{spec}}^2}}, \quad (17)$$

where  $\beta_{\text{spec}}$  is the relativistic velocity of the spectator in the overall center-of-mass system. We assume:  $\beta_{\text{spec}} = \beta_{A_i/\text{CM}}$ , where the latter is velocity of the projectile/target in the overall CM system. Then:

$$\beta_{\text{spec}} = \frac{\sqrt{s/4 - m_N^2}}{\sqrt{s}/2}. \quad (18)$$

For the maximal NA49 energy  $\sqrt{s_{NN}} = 17.3$  GeV we get  $\beta_{\text{spec}} = 0.9942$  and the dilatation factor is of about 10. The spectators could live even more than 40000 fm/c.

Thus, we conclude that the spectator systems, whatever the final fate is (ER or fission), live long enough to cause the electromagnetic effect observed in [40, 41].

<sup>3</sup> The charge of the ER is in 90% of the cases above 70, independent of the models used (note the logarithmic scale in Fig. 11 (a))

<sup>4</sup> The corresponding time in the overall center-of-mass system is larger due to Lorentz dilatation by about a factor of 10, see left-side  $y$ -axis.

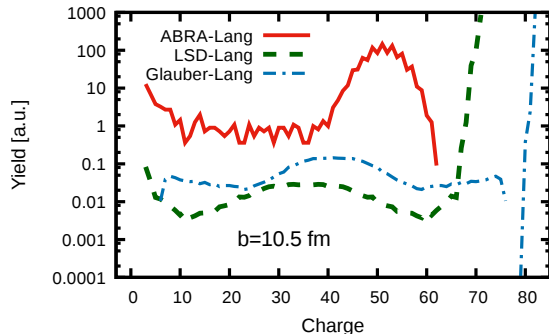


FIG. 13: (Color on-line) Charge distribution of the products (ER and fission fragments) predicted with three abrasion models combined with the same Langevin decay code, for the restricted range of impact parameter  $b \in (10-11)$  fm.

In the experiments such as NA49 or NA61 the colliding heavy ions have energy  $2 \text{ GeV} \leq \sqrt{s_{NN}} \leq 17.3 \text{ GeV}$ . The experiments at SPS concentrate on measuring rapidity and transverse momentum distributions of pions, kaons, nucleons, etc. They can also measure residues of the collisions in very forward direction (see e.g. [38, 39]). So far such measurements are done independently. We do not know whether they can be done in coincidence which would provide new information on how the participant and spectator systems are correlated. Also, it could enlight the predictions of this work.

#### D. Decay at specific impact parameter

The investigation of Ref. [2] about the influence of the spectator electromagnetic field on pion trajectories was performed at fixed impact parameter  $b \approx 10.5$  fm. In this paragraph we therefore sort the calculations according to impact parameter. In practice, we do restrict to those predictions corresponding to  $b \in (10-11)$  fm.

The outcome of the first abrasion stage, in terms of prefragment properties, is very different depending on the abrasion model used. In the geometrical macroscopic picture ('sphere-cylinder scenario'), the prefragment predicted in this impact parameter slice is peaked around  $^{181}\text{Lu}$  with an excitation energy slightly less than 100 MeV. For the Glauber model, very few nucleons are removed: the remnant is sharply centered around  $^{206}\text{Pb}$  with  $E^* \in (20-50)$  MeV. Finally, according to ABRA, the prefragment mass is characterized by a wider distribution around  $A \approx 170$ , similar to the geometrical macroscopic approach, but with a much larger ( $E^*$  above 500 MeV).

The outcome of the three abrasion models were combined with the Langevin code in order to compute the decay of the hot prefragments, as explained in the previous section, and then sorted according to  $b \in (10-11)$  fm. The resulting distributions for the final product charge are shown in Fig. 13. Whereas ER dominate the distribu-

tion for LSD-Lang and Glauber-Lang, fission is the main decay channel for ABRA-Lang, due to the much higher excitation energy involved. The fission time amounts to  $\tau_{spec} \sim 1792 \text{ fm/c}$ ,  $\sim 471 \text{ fm/c}$ , and  $\sim 711273 \text{ fm/c}$  for LSD-Lang, ABRA-Lang and Glauber-Lang, respectively. All these times are sufficiently large for the electromagnetic effects predicted in Ref. [2] to be active and affect the trajectory of the pions emitted from the fireball. That is, for those events which do not produce a final heavily-charged ER, and for which fission instead takes place, the decay by fission is slow enough for having at hand a still very heavy charge for quite some time and which influences the pion trajectories and momentum distributions.

## V. CONCLUSIONS

The decay of the heavy excited spectator remnants produced in peripheral heavy-ion collisions at ultra-relativistic energies, and which has received a poor attention so far, is investigated with an innovative theoretical framework. Within the picture of the well-established two-stage reaction scenario, three abrasion models - borrowed from the relativistic beam energy domain, were combined with a dynamical model based on the stochastic Langevin approach - popular in the physics at Coulomb barrier energies for modeling the competition between evaporation and fission. Statistical-model calculations with the ABRABLA code, which software has shown very powerful for collisions of relativistic heavy ions, are considered as well.

Comparison between various model combinations for the first and second stage of the reaction allows to study the influence of the predicted prefragment spectator mass and excitation energy after abrasion, as well as the influence of the modeling of the excited prefragment decay, on the final product charge distribution. The ABRABLA code is observed to describe the corresponding available experimental data rather well, demonstrating its good extrapolation properties in the ultra-relativistic domain where it was never tested. Also, the dynamical calculation computed within the Langevin approach, and combined with a reasonable abrasion model, shows a rather promising tool for modeling the decay of the heaviest spectators produced in peripheral collisions.

The main asset of the here-proposed Langevin approach lies in the possibility to predict the time evolution of the spectator, in contrast to purely statistical codes. Recent theoretical studies suggest that understanding this evolution may be crucial to consistently explain the pion spectra observed in the energy domain typical of the future CERN SPS or RHIC facilities. The time scale for the decay of the spectator predicted with our new theoretical framework within this field is consistent with the presence of a heavy system that lives long enough to impact the trajectory of the pions from the fireball region by its strong electromagnetic field.

The present work shows the widespread potential for the implementation of the stochastic Langevin approach. At Coulomb barrier energies, the method was successfully used to get insight into nuclear dynamics, and more specifically friction of nuclear matter [29, 30, 42]. The approach also demonstrated to be a pre-requisite tool for un-ambiguously understanding the dynamics and subtle time evolution of nuclei across the Businaro-Gallone transition [37]. This exploratory work suggests that it can be an interesting approach for the ultra-relativistic energy community for describing the fate of peripheral collisions. Beside the aspect of pion trajectory mentioned in this work, combining such studies with work on abrasion-induced reactions at relativistic energy may also be a relevant playground to investigate the disappearance of friction effects in the entrance channel of the reaction with increasing beam energy. The latter is expected to lead to lower excitation energy of the spectator, which would surely affect its time evolution and decay.

### Acknowledgements

This work was partially supported by the Polish National Science Centre under Contract No. 2013/08/M/ST2/00257 (LEA COPIGAL) (Project No. 18) and IN2P3-COPIN (Projects No. 12-145, 09-146), and by the Russian Foundation for Basic Research (Project No. 13-02-00168). We are very thankful to Dr. Aleksandra Kelic-Heil for calculations with the ABRABLA code and related analysis. We are also indebted to Andrzej Rybicki for discussion about experiments at the CERN SPS.

### Appendix A: Surface and volume calculations

- The volume of the sphere with radius  $R_{\text{sphere}} = 1.2A^{1/3}$  fm:

$$V_{\text{sphere}}(R_{\text{sphere}}) = \frac{4}{3}\pi R_{\text{sphere}}^3, \quad (\text{A1})$$

with the surface of the sphere:

$$S_{\text{sphere}}(R_{\text{sphere}}) = 4\pi R_{\text{sphere}}^2. \quad (\text{A2})$$

- The volume of the spherical cap reads:

$$V_{\text{cap}}(b) = \pi h^2(b) R_{\text{sphere}} - \frac{\pi}{3} h^3, \quad (\text{A3})$$

where  $h(b)$  is the height of the cap;  $a(b)$  - radius of the cap.  $b$  - impact parameter. The analytical formula for the surface of the spherical reads:

$$S_{\text{cap}}(b) = 2\pi h(b) R_{\text{sphere}}. \quad (\text{A4})$$

- For the 'sphere-plane' (s-p) scenario the surface and the volume are:

$$S^{\text{s-p}}(b) = S_{\text{sphere}} - S_{\text{cap}}(b) + a^2(b)\pi, \quad (\text{A5})$$

$$V^{\text{s-p}}(b) = V_{\text{sphere}} - V_{\text{cap}}(b). \quad (\text{A6})$$

- For the 'sphere-sphere' (s-s) scenario the surface and the volume are:

$$S^{\text{s-s}}(b) = S_{\text{sphere}}, \quad (\text{A7})$$

$$V^{\text{s-s}}(b) = V_{\text{sphere}} - 2V_{\text{cap}}(b). \quad (\text{A8})$$

The impact parameter is:

$$b^{\text{s-p}}(b) = 2R_{\text{sphere}} - h \quad (\text{A9})$$

$$b^{\text{s-s}}(b) = 2(R_{\text{sphere}} - h) \quad (\text{A10})$$

- The 'sphere-cylinder' (s-c) scenario is more complicated as there are no corresponding analytical formulas.

Our method to obtain the surface and volume of the spectator are presented below.

Let us consider characteristic points shown in Fig. 14:

$$x_1 = R_1 + R_2 - b \quad (\text{center of cylinder}), \quad (\text{A11})$$

$$x_2 = x_1 - R_2 = R_1 - b \quad (\text{A12})$$

position of the inner surface for  $z = 0$ ,

$$x_3 = \frac{R_1^2 - R_2^2 + x_1^2}{2x_1}, \quad (\text{A13})$$

position of extremal meeting point 'sphere - cylinder'

$$z_3 = \sqrt{R_1^2 - x_3^2}, \quad (\text{A14})$$

position of crossing point of sphere and cylinder.

The deformed spectator is cut in the  $z$  direction with slices of  $\Delta z$  long. In the plane  $(x, y)$  the shape of the slice looks like the circle without circular sector. The length of the chord, can be estimated with angle  $\theta$

$$\rho(z) = \rho_{z_i} = \sqrt{R_1^2 - z_i^2}, \quad (\text{A15})$$

radius of the shell for various  $z$  - coordinates,

$$y_3 = \sqrt{\rho_{z_i}^2 - x_3^2}, \quad (\text{A16})$$

$$\sin(\theta_i/2) = \frac{y_3}{\rho_{z_i}}, \quad (\text{A17})$$

angle of the circular segment.

The surface of the deformed spectator:

$$S^{\text{iner.surf.}}(b) = \sum_i 2y_3 \Delta z, \quad (\text{A18})$$

$$S^{\text{circ.seg.}}(b) = \frac{\rho_{z_i}^2}{2}(\theta_i - \sin \theta_i), \quad (\text{A19})$$

$$S^{\text{s-c}}(b) = \sum_i (\rho_{z_i} + \rho_{z(i-1)})(1 - \theta_i) \Delta z, \quad (\text{A20})$$

$$V^{\text{s-c}}(b) = \sum_i (\pi \rho_{z_i}^2 - S^{\text{iner.surf.}}(b)) \Delta z, \quad (\text{A21})$$

where:  $S^{\text{circ.seg.}}$  - surface of circular segment,  $S^{\text{iner.surf.}}$  is the surface of contact plane between the sphere and the cylinder.

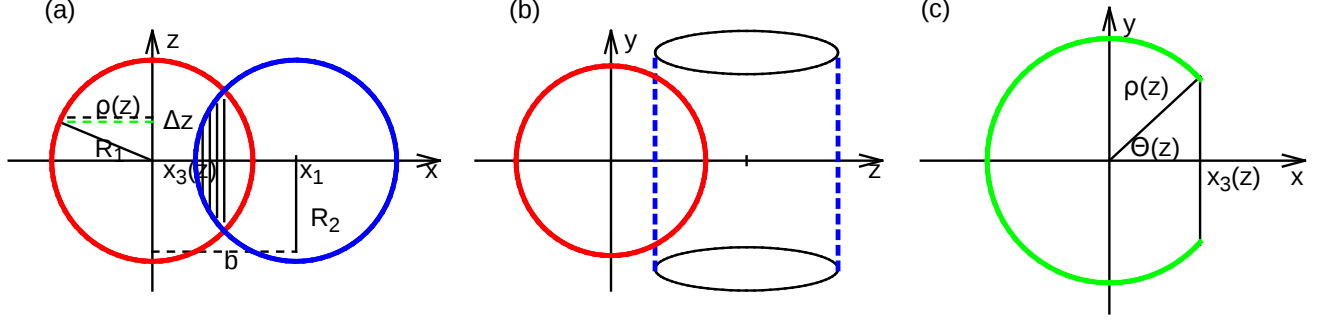


FIG. 14: The cuts of the sphere in various planes. The red circle present the spectator-target, blue-projectile, green- one layer in z-direction.

- The radius of a reference sphere (after collapsing deformed spectator):

$$R^{s-p}(b) = \left( \frac{3V^{s-p}(b)}{4\pi} \right)^{1/3}, \quad (\text{A22})$$

$$R^{s-s}(b) = \left( \frac{3V^{s-s}(b)}{4\pi} \right)^{1/3}, \quad (\text{A23})$$

$$R^{s-c}(b) = \left( \frac{3V^{s-c}(b)}{4\pi} \right)^{1/3}. \quad (\text{A24})$$

The surface of the reference spheres:

$$S_{spect}^{s-p}(b) = \frac{4}{3}\pi(R^{s-p}(b))^3, \quad (\text{A25})$$

$$S_{spect}^{s-s}(b) = \frac{4}{3}\pi(R^{s-s}(b))^3, \quad (\text{A26})$$

$$S_{spect}^{s-c}(b) = \frac{4}{3}\pi(R^{s-c}(b))^3. \quad (\text{A27})$$

- The geometrical surface factor, which enters into the deformation energy formula (Eq. (B1)), repeating Eq. (B6):

$$B_{\text{surf.}}(def) = \frac{S(def)}{S(\text{sphere})}. \quad (\text{A28})$$

For the different scenarios considered:

$$B_{\text{surf.}}^{s-p}(b) = \frac{S^{s-p}(b)}{S_{spect}^{s-p}(b)}, \quad (\text{A29})$$

$$B_{\text{surf.}}^{s-s}(b) = \frac{S^{s-s}(b)}{S_{spect}^{s-s}(b)}, \quad (\text{A30})$$

$$B_{\text{surf.}}^{s-c}(b) = \frac{S^{s-c}(b)}{S_{spect}^{s-c}(b)}. \quad (\text{A31})$$

$$(\text{A32})$$

- The radius of the new sphere, its surface and geometrical factor can be written for  $i = p, s, c$  as:

$$R^{s-i}(b) = \left( \frac{3V^{s-i}(b)}{4\pi} \right)^{1/3}, \quad (\text{A33})$$

$$S_{spect}^{s-i}(b) = \frac{4}{3}\pi(R^{s-i}(b))^3, \quad (\text{A34})$$

$$B_{\text{surf.}}^{s-i}(b) = \frac{S^{s-i}(b)}{S_{spect}^{s-i}(b)}. \quad (\text{A35})$$

$$(\text{A36})$$

- Also the estimation of the mass and charge of the spectator for  $i = p, s, c$  is calculated as:

$$A^{s-i}(b) = A_{Pb} \frac{V^{s-i}(b)}{V_{\text{sphere}}}, \quad (\text{A37})$$

$$Z^{s-i}(b) = Z_{Pb} \frac{V^{s-i}(b)}{V_{\text{sphere}}}. \quad (\text{A38})$$

## Appendix B: Details of the Lublin-Strasbourg Drop model

The macroscopic energy from the Lublin-Strasbourg Drop (LSD) model [13, 14] used in this context has the following form for nucleus with the mass number  $A$  and charge  $Z$ :

$$E_{\text{total}}(A, Z; def) = E(A, Z) + E_{\text{Coul.}}(A, Z; def) + E_{\text{surf.}}(A, Z; def) + E_{\text{curv.}}(A, Z; def) \quad (\text{B1})$$

where  $def$  are the deformation parameters depending on the chosen parametrization of the shape. Above we find  $E_{\text{Coul.}}(A, Z; def)$  - deformation-dependent Coulomb electrostatic energy term, the surface,  $E_{\text{surf.}}(A, Z; def)$ , and curvature,  $E_{\text{curv.}}(A, Z; def)$  terms. The first term on the right-hand side of Eq. (B1) denotes by definition the combined deformation-independent terms:

$$E(A, Z) = ZM_{\text{H}} + (A - Z)M_{\text{n}} - 0.00001433 Z^{2.39} + E_{\text{vol.}}(A, Z) + E_{\text{cong.}}(A, Z), \quad (\text{B2})$$

where the term proportional to  $Z^{2.39}$  is the binding energy of the electrons whereas the other two terms represent  $Z$  masses of the Hydrogen atom and  $(A - Z)$

masses of the neutron, respectively. The deformation-independent congruence energy term is  $E_{\text{cong.}}(A, Z)$ .

The volume energy is parametrized as:

$$E_{\text{vol.}}(Z, A) = b_{\text{vol.}} (1 - \kappa_{\text{vol.}} I^2) A, \quad (\text{B3})$$

where  $I = (A - 2Z)/(A + 2Z)$  is introduced for brevity. All the parameters appearing implicitly in Eq. (B1), such as  $b_{\text{vol.}} = -15.4920$  MeV and  $\kappa_{\text{vol.}} = 1.8601$  and the ones that appear below, are taken from [13].

The Coulomb LDM term reads:

$$E_{\text{Coul.}}(A, Z; def) = \frac{3}{5} e^2 \frac{Z^2}{r_0^{ch} A^{1/3}} B_{\text{Coul.}}(def) - C_4 \frac{Z^2}{A}, \quad (\text{B4})$$

with electric charge unit denoted as  $e$ , and the so-called charge radius parameter  $r_0^{ch} = 1.21725$  fm,  $C_4 = 0.9181$  MeV. The term proportional to  $Z^2/A$  represents the nuclear charge-density diffuseness-correction whereas the deformation dependent term,  $B_{\text{Coul.}}(\alpha)$ , denotes the Coulomb energy of a deformed nucleus normalized to that of the sphere with the same volume.

The surface energy in the LDM form reads:

$$E_{\text{surf.}}(A, Z; def) = b_{\text{surf.}} (1 - \kappa_{\text{surf.}} I^2) A^{2/3} B_{\text{surf.}}(def), \quad (\text{B5})$$

where  $b_{\text{surf.}} = 16.9707$  MeV and  $\kappa_{\text{surf.}} = 2.2938$ . The deformation dependent term is defined as the surface energy of a deformed nucleus normalized to that of the sphere of the same volume:

$$B_{\text{surf.}}(def) = \frac{S(def)}{S(sphere)}. \quad (\text{B6})$$

The curvature term is given by:

$$E_{\text{curv.}}(A, Z; def) = b_{\text{curv.}} (1 - \kappa_{\text{curv.}} I^2) A^{1/3} B_{\text{curv.}}(def) \quad (\text{B7})$$

with

$$B_{\text{curv.}}(def) = \int_0^\pi d\vartheta \int_0^{2\pi} d\varphi \left[ \frac{1}{R_1(\vartheta, \varphi; def)} + \frac{1}{R_2(\vartheta, \varphi; def)} \right], \quad (\text{B8})$$

where  $R_1$  and  $R_2$  are deformation-dependent principal radii of the nuclear surface at the point-position defined by spherical angles  $\vartheta$  and  $\varphi$ ,  $b_{\text{curv.}} = 3.8602$  MeV and  $\kappa_{\text{curv.}} = -2.3764$ . The LSD parameters have been fitted to all known experimental masses and well reproduced the fission barriers.

- 
- [1] A. Rybicki, A. Szcurek, arXiv:1405.6860v1 (2014)
  - [2] A. Rybicki, A. Szcurek, Phys. Rev. C **75**, 054903 (2007)
  - [3] A. Rybicki, A. Szcurek, Phys. Rev. C **87**, 054909 (2013)
  - [4] J.D. Bowman, W.J. Swiatecki, C.E. Tsang, Lawrence Berkley Laboratory report **LBL**, 2908 (1973)
  - [5] D.J. Morrissey, W.R. Marsh, R.J. Otto, W. Loveland, G.T. Seaborg, Phys. Rev. C **18**, 1267 (1978)
  - [6] W.J. Swiatecki, unpublished (1976)
  - [7] A. Szcurek, M. Kielbowicz, A. Rybicki, Phys. Rev. C **95**, 024908 (2017)
  - [8] J.J. Gaimard, K.H. Schmidt, Nucl. Phys. A **531**(3), 709 (1991)
  - [9] A. Kelic, M. Ricciardi, K.H. Schmidt, arXiv:0906.4193v1 (2008)
  - [10] H. Schlagheck, Nuclear Physics A **663**, 725c (2000)
  - [11] J. Hüfner, K. Schäfer, B. Schürmann, Phys. Rev. C **12**, 1888 (1975)
  - [12] G.D. Westfall, J. Gosset, P.J. Johansen, A.M. Poskanzer, W.G. Meyer, H.H. Gutbrod, A. Sandoval, R. Stock, Phys. Rev. Lett. **37**, 1202 (1976)
  - [13] K. Pomorski, J. Dudek, Phys. Rev. C **67**, 044316 (2003)
  - [14] J. Dudek, K. Pomorski, N. Schunck, N. Dubray, Eur. Phys. J. A **20**, 165 (2004)
  - [15] L.F. Oliveira, R. Donangelo, J.O. Rasmussen, Phys. Rev. C **19**, 826 (1979). DOI 10.1103/PhysRevC.19.826. URL <https://link.aps.org/doi/10.1103/PhysRevC.19.826>
  - [16] K.H. Schmidt, T. Brohm, H.G. Clerc, M. Dornik, M. Fauerbach, H. Geissel, A. Grewe, E. Hanelt, A. Jung-hans, A. Magel, W. Morawek, G. Mnzenberg, F. Nickel, M. Pftzner, C. Scheidenberger, K. Smmerer, D. Vieira, B. Voss, C. Ziegler, Physics Letters B **300**(4), 313 (1993)
  - [17] K. Mazurek, P.N. Nadtochy, A. Szcurek, The Acta Physica Polonica B Proc. Supp. **10**, 113 (2017)
  - [18] W.D. Myers, W.J. Swiatecki, Ark. Phys. **36**, 343 (1967)
  - [19] H.J. Krappe, J.R. Nix, A.J. Sierk, Phys. Rev. C **20**, 992 (1979)
  - [20] P. Möller, A.J. Sierk, A. Iwamoto, Phys. Rev. Lett. **92**, 072501 (2004)
  - [21] L.G. Moretto, P.T. Lake, L. Phair, J.B. Elliott, Phys. Rev. C **86**, 021303 (2012)
  - [22] M. de Jong, A.V. Ignatyuk, K.H. Schmidt, Nucl. Phys. A **613**, 435 (1997)
  - [23] Nuclear Physics A **710**, 157 (2002)
  - [24] J. Dobaczewski, W. Nazarewicz, T.R. Werner, Zeitschrift für Physik A Hadrons and Nuclei **354**(1), 27 (1996)
  - [25] T. Ericson, Adv. Phys. **9**, 425 (1960)
  - [26] H.A. Kramers, Physica **7**, 284 (1940)
  - [27] Y. Abe, S. Ayik, P.G. Reinhard, E. Suraud, Phys. Rep. **275**, 49 (1996)
  - [28] P. Fröbrich, I.I. Gontchar, Physics Reports **292**, 131 (1998)
  - [29] K. Mazurek, P.N. Nadtochy, E.G. Ryabov, G.D. Adeev, Eur. Phys. J. A **53**(4), 79 (2017)
  - [30] G.D. Adeev, A.V. Karpov, P.N. Nadtochy, D.V. Vanin, Phys. Part. Nucl. **36**, 378 (2005)
  - [31] P.N. Nadtochy, G.D. Adeev, Phys. Rev. C **72**, 054608 (2005)
  - [32] M. Brack, J. Damgaard, A.S. Jensen, H.C. Pauli, V.M. Strutinsky, C.Y. Wong, Rev. Mod. Phys. **44**, 320 (1972)
  - [33] K.T.R. Davies, A.J. Sierk, J.R. Nix, Phys. Rev. C **13**, 2385 (1976)
  - [34] J. Blocki, Y. Boneh, J.R. Nix, J. Randrup, M. Robel,

- A.J. Sierk, W.J. Swiatecki, *Ann. Phys. (N. Y.)* **113**, 330 (1978)
- [35] G. Chaudhuri, S. Pal, *Phys. Rev. C* **63**, 064603 (2001)
- [36] N.D. Mavlitov, P. Fröbrich, I.I. Gontchar, *Z. Phys. A* **342**, 195 (1992)
- [37] K. Mazurek, C. Schmitt, P.N. Nadtochy, A.V. Cheredov, *Phys. Rev. C* **94**, 064602 (2016)
- [38] S. Cecchini, G. Giacomelli, M. Giorgini, G. Mandrioli, L. Patrizii, V. Popa, P. Serra, G. Sirri, M. Spurio, *Nucl. Phys. A* **707**(3), 513 (2002)
- [39] H. Dekhissi, G. Giacomelli, M. Giorgini, G. Mandrioli, S. Manzoor, L. Patrizii, V. Popa, P. Serra, V. Togo, *Nucl. Phys. A* **662**, 207 (2000)
- [40] A. Rybicki, *J. of Phys. G: Nucl. and Part. Phys.* **30**(8), S743 (2004)
- [41] A. Rybicki, *Acta Phys. Pol. B* **42**, 867 (2011)
- [42] P.N. Nadtochy, E.G. Ryabov, A.E. Gegechkori, Y.A. Anischenko, G.D. Adeev, *Phys. Rev. C* **85**, 064619 (2012)